

New Perspectives on Turbulent Mixing Induced by Raleigh-Taylor and Richtmyer-Meshkov Instabilities

*Y. Zhou, B.A. Remington, S.G. Glendinning, A. Dimits,
A.C. Buckingham, H.F. Robey, A.W. Cook, T.T. Clark, G.
Zimmerman, E.W. Burke, T.A. Peyser, W. Cabot, D.
Eliason*

U.S. Department of Energy

Lawrence
Livermore
National
Laboratory

This article was submitted to
44th Annual Meeting of the Division of Plasma Physics, Orlando,
Florida, November 11-15, 2002

October 30, 2002

DISCLAIMER

This document was prepared as an account of work sponsored by an agency of the United States Government. Neither the United States Government nor the University of California nor any of their employees, makes any warranty, express or implied, or assumes any legal liability or responsibility for the accuracy, completeness, or usefulness of any information, apparatus, product, or process disclosed, or represents that its use would not infringe privately owned rights. Reference herein to any specific commercial product, process, or service by trade name, trademark, manufacturer, or otherwise, does not necessarily constitute or imply its endorsement, recommendation, or favoring by the United States Government or the University of California. The views and opinions of authors expressed herein do not necessarily state or reflect those of the United States Government or the University of California, and shall not be used for advertising or product endorsement purposes.

This is a preprint of a paper intended for publication in a journal or proceedings. Since changes may be made before publication, this preprint is made available with the understanding that it will not be cited or reproduced without the permission of the author.

This report has been reproduced directly from the best available copy.

Available electronically at <http://www.doe.gov/bridge>

Available for a processing fee to U.S. Department of Energy
and its contractors in paper from
U.S. Department of Energy
Office of Scientific and Technical Information
P.O. Box 62
Oak Ridge, TN 37831-0062
Telephone: (865) 576-8401
Facsimile: (865) 576-5728
E-mail: reports@adonis.osti.gov

Available for the sale to the public from
U.S. Department of Commerce
National Technical Information Service
5285 Port Royal Road
Springfield, VA 22161
Telephone: (800) 553-6847
Facsimile: (703) 605-6900
E-mail: orders@ntis.fedworld.gov
Online ordering: <http://www.ntis.gov/ordering.htm>

OR

Lawrence Livermore National Laboratory
Technical Information Department's Digital Library
<http://www.llnl.gov/tid/Library.html>

This work was performed under the auspices of the U.S. Department of Energy by the University of California, Lawrence Livermore National Laboratory under contract No. W-7405-Eng-48.

**New perspectives on turbulent mixing induced by Rayleigh-Taylor
and Richtmyer-Meshkov instabilities***

Ye Zhou, B.A. Remington, S.G. Glendinning, A. Dimits,
A.C. Buckingham, H.F. Robey, A.W. Cook, T.T. Clark[#],
G. Zimmerman, E.W. Burke, T.A. Peyser, W. Cabot, D. Eliason

Lawrence Livermore National Laboratory

University of California, Livermore, CA 94551

[#]Los Alamos National Laboratory

Abstract

Turbulent hydrodynamic mixing induced by the Rayleigh-Taylor (RT) and Richtmyer-Meshkov (RM) instabilities occurs in settings as varied as exploding stars (supernovae), inertial confinement fusion (ICF) capsule implosions, and macroscopic flows on fluid dynamics facilities such as shock tubes. We have developed a quantitative description of turbulence from the onset to the asymptotic end-state. Our treatment, based on a combined approach of theory, direct numerical simulation (DNS), and experimental data analysis, has broad generality. We will report two key areas in our progress. First, we have developed a robust, easy to apply criteria for the mixing transition in a time-dependent flow. This allows an assessment of whether flows, be they from supernova explosions or ICF experiments, should be turbulent or not. Second, we inspect the structure, scaling and spectra of the Rayleigh-Taylor (RT) and Richtmyer-Meshkov (RM) instabilities induced flows.

I. Introduction and summary

Turbulent hydrodynamic mixing induced by the Rayleigh-Taylor (RT) [1] and Richtmyer-Meshkov (RM) [2] instabilities occurs in settings as varied as supernova explosions [3-5], inertial confinement fusion (ICF) capsule implosions [6], and macroscopic flows on fluid dynamics facilities such as shock tubes. The Rayleigh-Taylor instability (RTI) occurs when light fluid supports a denser fluid in an accelerated field. The impulsive version of the Rayleigh-Taylor instability, the Richtmyer-Meshkov instability (RMI), is generated when a perturbed interface between two fluids is impulsively accelerated, typically by a shock wave. These instabilities are important to our understanding of many astrophysical phenomena and play important roles in ICF.

We have for the first time developed a quantitative description of turbulence from the onset to the asymptotic end-state. Our treatment, based on a combined approach of theory, direct numerical simulation (DNS), and experimental data analysis has broad generality. We will report several key areas in our progress.

First, we have developed a robust, easy to apply criteria for the mixing transition in a time-dependent flow. This allows an assessment of whether flows should be turbulent or not, be they from supernova explosions or ICF experiments. Note that the spatial and time scales in these diverse settings can differ by as much as 14-16 orders of magnitude, yet our theoretical framework still applies.

Second, we have investigated the energy spectra, scaling and structure of RT and RM flows. The energy spectra appropriate for RT and RM flows are obtained and shown to be different from that of classical Kolmogorov spectrum. The late-time evolution of the RMI

mixing layer is studied from the viewpoint of isotropic turbulence. Analogies with isotropic turbulence suggested that both the bubble-side and spike-side widths of the mixing layer should evolve as a power law in time, with the same power-law exponent for both sides but with different virtual time origins and coefficients for each side. The analogy also bounds the power-law exponent between $2/7$ and $2/5$. The structure and energy transfer processes within the mixing layer are investigated using DNS.

II. Mixing transition in time-dependent flows

Many experiments have been conducted in classical fluid dynamics facilities, shock tubes, and laser facilities (such as the Omega laser) to understand the complex phenomena associated with RTI and RMI flows. These experiments address different aspects of the physics of Rayleigh-Taylor and Richtmyer-Meshkov instabilities. Due to diagnostic limitations typical measurements are of the growth of the mixing zone width. While these widths (of the bubble and spike fronts, individually or combined) are usually measured, it is difficult to know whether or not a particular experiment has reached the mixing transition. This type of information cannot be easily obtained from flow visualizations.

The mixing transition concept for *stationary* fluid flows, developed recently by Dimotakis [7], refers to the transition to a turbulent state in which the flow drives rapid mixing at the molecular scale. This turbulent state leads to rapid dissipation of momentum and of concentration fluctuations (mixing). The classical Kolmogorov theory [8] assumes that in the inertial range, the dynamics at an intermediate scale, λ , cannot be influenced by the outer, low

frequency scales, δ , where turbulent energy is produced, nor can it be influenced by the inner, high frequency, viscous dissipation scales (represented by the Kolmogorov microscale,

$\lambda_K = C \nu^3 / \epsilon$, where ν is the kinematic viscosity and ϵ is the dissipation rate)

$$\lambda_K \ll \lambda \ll \delta.$$

Dimotakis [7] proposed that the extent of the effective inertial range could be narrowed to

$$\lambda_K < \lambda_v \ll \lambda \ll \lambda_L < \delta,$$

Here the lower-limit of the inertial range is the inner viscous scale $\lambda_v = 50\lambda_K$, where the

Kolmogorov microscale can be rewritten as $\lambda_K = \delta \text{Re}^{-3/4}$. Note that Re is the outer-scale

Reynolds number ($\text{Re} = \frac{U\delta}{\nu}$ where U is a characteristic velocity). The upper-limit of the

inertial range is the Liepmann-Taylor scale $\lambda_L = 5\lambda_T$, where $\lambda_T = \delta \text{Re}^{-1/2}$ the well known

Taylor correlation microscale [8]. For RTI and RMI induced flows, the outer-scale δ is given

by the mixing zone width h so that

$$\text{Re} = \frac{hU}{\nu}.$$

We have extended the stationary mixing transition to time-dependent flows and applied it to a wide range of experiments [9,10]. For time-dependent flows, the mixing transition may occur at a particular time. In designing and interpreting experiments for time-dependent flows, it is extremely desirable to be able to estimate the time required to achieve the mixing transition state. In this section, we apply the mixing transition concept to a selection of RTI and RMI experiments. This broad survey will be useful for guiding future experimental designs.

A. Mixing transition criterion for time-dependent flows

In this section, we summarize the mixing transition criterion for time-dependent flows, in a form relevant to the development of a mixing layer initiated by RTI or RMI. Here, the outer-scale δ and the outer-scale Reynolds numbers are both functions of time. The Liepmann-Taylor scale essentially describes the internal laminar vorticity growth layer generated by viscous shear along the boundaries of a large-scale feature of size δ . The temporal development of such a laminar viscous layer is well known to go as $(\nu t)^{1/2}$ (Stokes [11], Rayleigh [1], Lamb [12]). In the RTI and RMI induced flow, the Liepmann-Taylor scale increases with time as a viscous diffusion layer

$$\lambda_D \equiv C \times (\nu t)^{1/2}.$$

Hence, the upper bound of the developing inertial range is the smaller of the Liepmann-Taylor scale, λ_L and λ_D . Here the coefficient of the diffusion layer, C , was suggested as $C \approx \sqrt{15}$ both for isotropic, homogeneous turbulence [13] and for steady parallel flows, and as $C \equiv 5$ [14] for laminar boundary layer flows (following the Liepmann-Taylor constant by Dimotakis [7]).

The Kolmogorov inertial range is presumed to be established when the evolution of the large-scale, $\min\{\lambda_D, \lambda_L\}$, is decoupled from the inner viscous scale, λ_ν . For time-dependent flows, the mixing transition is achieved when a range of scales exists such that the temporally evolving upper bound $[\min\{\lambda_D, \lambda_L\}]$ is significantly larger than the temporally evolving lower bound, λ_ν . Thus, the mixing transition occurs if and when the inequality [9,10]

$$\min\{\lambda_L(t), \lambda_D(t)\} > \lambda_\nu(t) \equiv 50\lambda_k(t) \quad (1)$$

is satisfied.

B. Rayleigh-Taylor Experiments

1. AWE Rocket-Rig Experiment

The AWE experiments used solid fuel rocket motors to achieve high and approximately constant acceleration over a distance of about 1.5 m. A 3D experimental tank of dimension 150 mm^3 was driven by the rocket motors to move vertically downwards between two parallel steel rods. To obtain the highest accelerations, two rocket motors, fired simultaneously, were used for propulsion. The motion of the tank was stopped at the end by means of an expanded polystyrene cushion. For a detailed discussion of the rocket rig facility and a complete list of experiments, see Read [15] and Youngs [16].

In this paper, we consider experiment #33 of Read and Youngs [17], which used NaI solution ($\rho = 1.88$) and pentane ($\rho = 0.63$). The Atwood number was 0.5 and the acceleration of the experiment was 27 times that of gravity, that is $g = 27g_0$. The kinematic viscosities for the NaI solution and pentane are $0.017 \text{ cm}^2/\text{s}$ and $0.0037 \text{ cm}^2/\text{s}$, respectively.

In Fig. 1 (a), we show the development of the mixing zone, $h = h_b + h_s$, versus time. The values of the Reynolds number, $\text{Re} = h\dot{h}/\nu$, for both NaI (black) and pentane (red) are illustrated in Fig. 1 (b), showing that they reach large values, $\text{Re} \geq 5 \times 10^4$, over the duration of the experiment. In Fig. 1 (c), we plot the two sides of Eq. (1), the inequality for the mixing transition requirement. The dashed lines show $\min\{\lambda_L(t), \lambda_D(t)\}$ and the solid lines show $\lambda_v(t)$ for NaI (black) and pentane (red). This figure shows that the condition for the mixing transition is satisfied for both the NaI solution and the pentane quite early in the experiment at $t \geq 38 \text{ ms}$, so we conclude that this AWE rocket rig experiment did indeed attain the mixing

transition. The fact that the curves for $\min\{\lambda_L(t), \lambda_D(t)\}$ and $\lambda_v(t)$ pass through each other therefore opening up an inertial range is a clear evidence of the mixing transition.

2. LLNL Linear Electric Motor

The linear electric motor (LEM) facility can provide constant or impulsive accelerations [18-19]. The system resembles a rail gun, but with augmentation coils, solid armatures, and open diagnostic access. The accelerator consists of two coils that produce most of the magnetic field and two pairs of the magnetic field and two pairs of linear rails that conduct the current in the sliding armatures. The brake consists of two linear “drums,” one stationary and one spring loaded, that press on the cell.

The Rayleigh-Taylor instability driven flow is produced using water (1 g/cm^3) and Freon (1.57 g/cm^3) with an Atwood number of 0.22. In Fig. 2 (a) we show the growth of the mixing layer versus time. The Reynolds numbers (Fig. 2 (b)) for both the water (black) and Freon (red) evolve to large values, $\text{Re} \geq 10^5$, and therefore the flow is expected to undergo a mixing transition. The large Reynolds numbers are consistent with Fig. 2 (c), which shows that both fluids can easily satisfy the mixing transition requirement after about 20 *msec*.

C. Richtmyer-Meshkov Experiments

The second part of this section focuses on applying the mixing transition criterion to time dependent flows by focusing on the RMI driven flows. Some special issues on applying the method to experiments on the Omega Laser facility at high temperature and pressure are discussed.

We next turn to some low Mach number shock tube experiments, which provide encouraging evidence of our ability to predict mixing transition times.

1. LANL Gas Curtain

The first RMI experiment to be discussed is that of Rightley et al. [20]. A detailed description of the facility can be found in Rightley et al. [20] and we will only give a brief summary. The 5.5 m shock tube has a square cross section with a side of 75 mm. The driver section, pressurized to 140 kPa gauge pressure before the shot, is separated from the rest of the tube at ambient pressure by a polypropylene diaphragm. A solenoid-actuated scalpel ruptures the diaphragm, producing a Mach 1.2 planar shock wave propagating in the air of the driven section. There is a temporal uncertainty inherent in the creation of the shock, so the test section diagnostics are triggered by the passage of the shock wave past piezoelectric pressure transducers mounted flush on the wall of the driven section.

A vertical curtain of SF_6 (pure or mixed with tracers) is injected through a nozzle in the top of the test section and removed through an exhaust plenum in the test section bottom. Both the injection nozzle and the exhaust plenum are flush with the test section wall. The contour of the injection nozzle imposes a perturbation on the cross section of the curtain. Interchangeable nozzles make it possible to create initial conditions containing one or more perturbation wavelengths. The velocity in the curtain is on the order of 10 cm/s. The direction of the SF_6 flow (downward) improves the curtain stability and two-dimensionality. It is shown in Figs. 3 (a)– (c) that the experiment achieves the mixing transition.

2. RMI experiment on Omega Laser

A RM experiment is an efficient way to achieve the mixing transition. In order to determine the Reynolds number, an appropriate value for the kinematic viscosity must be found for plasma flows of the type produced by experiments using the Omega laser.

The coupling is determined by the plasma parameter $\Gamma = Z^2 e^2 / (k_B T \lambda_i)$, where ($Z \cdot e$) is the ionic charge and $\lambda_i = (3/4\pi N_i)^{1/3}$ is the average inter-ionic distance (N_i is the ion number density in cm^{-3}). Γ is therefore a measure of the ratio of potential to kinetic energy of the plasma. For $\Gamma \ll 1$, the plasma ions are weakly coupled, and the formula of Braginskii [21]

$$\nu_i = 3.3 \times 10^{-5} \frac{\sqrt{A} T^{5/2}}{\ln(\Lambda) Z^4 \rho_i}$$

is applicable for the kinematic viscosity of the low density, high temperature plasma state where ionic coupling is weak. Here, ν is the kinematic viscosity in cm^2/s , T is the ion temperature measured in eV ($1\text{eV} = 11604 \text{ K}$), ρ is the density in g/cm^3 , and A and Z are the atomic weight and number, respectively. The function $\ln(\Lambda)$ is the Coulomb logarithm, a function of the temperature and degree of ionization (see the NRL Plasma Formulary [22]). For dense plasma, the more extensive viscosity model of Clerouin *et al.* [23] should be used instead. This new formulation is applicable over a wider range of temperatures and densities. For this model, the kinematic viscosity is given by

$$\nu (\text{cm}^2/\text{s}) = 6.55 \times 10^{-10} Z_{\text{eff}} m_i^{1/2} n_i^{5/6} \begin{cases} 1.1 \Gamma_{\text{eff}}^{-1.895}, & \Gamma_{\text{eff}} < 2 \\ \lambda I_1 + \frac{(1 + \lambda I_2)}{\lambda I_3}, & 2 < \Gamma_{\text{eff}} < 160 \end{cases}$$

Here the effective plasma coupling parameter for this mixture is

$$\lambda = \frac{4\pi}{3} (3\Gamma_{\text{eff}})^{3/2}$$

$$\Gamma_{\text{eff}} = \frac{e^2 \overline{Z^{1/3}} \overline{Z^{5/3}}}{a k_B T}, \quad \overline{Z^{5/3}} = x_1 Z_1^{5/3} + x_2 Z_2^{5/3}$$

where a is the mean ionic radius, k_B is the Boltzmann constant.

The laser driven shock tube experiment is conducted on the Omega Laser located at University of Rochester. A three dimensional illustration of the experimental setup is shown in Figures 4 (a) and (b).

Fig. 4 (c) illustrated the experimental radiographs. In the image, the location of the shock and the resulting bubble/spike mixing zone width at the plastic-foam interface are shown.. The density on either side of the density discontinuity is shown (Fig.4 (d)), indicating the time of the shock arrival at $t = 1$ ns. The Atwood number (Fig. 10 (e)), after the peak value around 0.9 at $t = 1$ ns, settled down to values between 0.4 – 0.6. The temperature is shown to be relatively low (Fig. 4 (f)). The ionization is also computed. The resulting plasma coupling parameter is obtained (Fig. 4 (g)). After the shock passage, the plasma coupling parameter is shown to be around 2 for the foam and between 4-10 for plastic. The relatively strong plasma coupling is a direct result of the low temperature and indicates that the Clerouin *et al.* formula should be applicable instead of that by Braginskii.

The important parameters needed for estimating time-dependent mixing transition are obtained. The kinematic viscosity (Fig. 4 (h)) is also plotted for both sides of the interface. After the passage of the shock, the kinematic viscosity of the carbon foam achieves at approximately $0.004 \text{ cm}^2 / \text{s}$, while the kinematic viscosity of the plastic decreases from $0.015 \text{ cm}^2 / \text{s}$ at $t = 1$ ns to $0.002 \text{ cm}^2 / \text{s}$. The mix width (Fig. 4 (i)), computed from the perturbation peak-to-valley amplitude vs time is also shown. An averaged Reynolds number can be deduced (Fig. 4 (j)). The

Reynolds number increases very rapidly to 2×10^5 upon the shock passage then decreases to values around 10^5 .

The inner viscous layer, $\lambda_v = 50\lambda_K$, is shown with a solid line (Fig. 4 (k)). The shear induced diffusion layer length scale, $\lambda_D = (15\nu t)^{1/2}$, is shown to be smaller than the inner viscous layer for entire duration of the experiment. This is a direct consequence of the low temperature and small kinematic viscosity of this experiment. The mixing transition is determined by a sufficient scale separation (see discussion in Sec. 2) between the smaller of the Liepmann-Taylor and viscous diffusion scales and the inner-viscous scale. Clearly, the mixing transition for this experiment does not take place.

Future experiments that follow the interface evolution to longer times will be necessary to be able to achieve the required spectral range separation development, and will be essential in verifying these results. The availability of megajoule-class lasers such as the National Ignition Facility extends the possibilities for the development of accelerated flows driven by strong shocks to be studied well into the fully turbulent regime.

III. Scaling, structure and spectra

In the early stage of both the RTI and RMI the growth of the initial perturbation gives rise to distinct spikes (of heavy material) and bubbles (of light material). In the nonlinear stage, bubble merger leads to an evolving spectrum different from the initial perturbation. Mode coupling (nonlinear interactions) effects broaden the spectrum of length scales. Velocity shear between the spikes and bubbles then leads to Kelvin-Helmholtz instabilities, which further broaden the

spectrum of scales creates higher spatial frequencies. At large Reynolds numbers a full range of scales develops from sizes comparable to the size of the system to those of the Kolmogorov viscous dissipation scale.

A. Energy spectrum

For RTI driven flows, the late time scaling of the width of the mixed region (h) is

$$h_i = \alpha_i A g t^2$$

where the Atwood number A is given by

$$A = \frac{\rho_1 - \rho_2}{\rho_1 + \rho_2}$$

and the subscript i indicates bubble ($i=b$) or spike ($i=s$), and g is the acceleration due to gravity. Since bubbles penetrate more slowly than spikes, two amplitudes for each dominant RTI mode are needed to determine the values of the constant α_i .

The outer-scale Reynolds number is defined by the extent of the mixing region

($h = h_b + h_s$) and its rate of growth, \dot{h} ,

$$\text{Re} = \frac{h \dot{h}}{\nu}.$$

Using direct numerical simulation (DNS) datasets, Cook & Zhou [24] plot the time-evolution of density (see Fig. 5) and show that the outer-scale Reynolds number grows roughly like t^3 , which is expected if $h \sim t^2$ and $\dot{h} \sim t$ (Fig. 6).

Inertial subrange energy spectra of RTI and RMI driven flows have been developed using extended Kolmogorov-Kraichnan phenomenology. Turbulence theories indicate that the energy flux is explicitly proportional to the external time scale τ_T and depends on the wave number and on the power of the omni-directional energy spectrum. In the inertial range, because energy is

conserved by the nonlinear interactions and a local cascade has been assumed, the energy flux becomes independent of the wave number k . A comprehensive analysis of the energy transfer and interacting scales has been carried out for homogeneous isotropic and anisotropic flows. Since there is no “leak” of energy in the inertial range, the energy flux (source) and dissipation rate ε (sink) assume the same. A simple dimensional analysis leads to

$$\varepsilon = C^2 \tau_T k^4 E^2(k)$$

where C is a dimensionless constant.

RTI and RMI flows are both anisotropic and inhomogeneous in the direction of gravity (RTI) and planar shock motion (RMI). This requires a generalization from the previous treatment of MHD and strongly rotational flows, which may be homogeneous and anisotropic.

A first step in this generalization procedure is to define the wave number k as $k = \sqrt{k_x^2 + k_y^2}$ assuming that z is the direction of gravity (for RTI) and of the planar shock wave motion (for RMI).

For RTI driven flow, the time scale can be constructed from the external acceleration, g ,

$$\tau_{RT} = (kgA)^{-1/2}$$

It is the time scale required for the change of dynamics from the classical Kolmogorov phenomena.

For turbulent flow induced by RTI, a direct application of $\tau_T = \tau_{RT}$ results in the kinetic energy spectrum [25]:

$$E(k, z) = C_{RT} (gA)^{1/4} \varepsilon(z)^{1/2} k^{-7/4},$$

where C_{RT} is a constant. The time-evolution of the two-dimensional energy spectrum, $E(k, z = 0, t = 0, 2, 4, 6)$, is plotted in Fig. 7. The spectrum is nonzero at $t = 0$ as a result of the initial diffusion velocities. The spectrum increases by several orders of magnitude as kinetic energy is deposited into the flow. The peak of the spectrum migrates toward lower wave numbers as bubbles and spikes merge to form larger structures. The spectrum also fills out at higher wave numbers as vortex stretching, pairing, break up, and bending dynamics transfer energy to smaller scales via mode coupling. Near the end of the simulation it appears that an inertial range is just beginning to form. Both the classical Kolmogorov $-5/3$ and Zhou's $-7/4$ power laws are shown on the figure for comparison to the data. The statistical fluctuations in the spectra (there are not many points in the Fourier annuli at lower wave numbers) are larger than the difference in slope between $k^{-7/4}$ and $k^{-5/3}$. Furthermore, there is no clear beginning to the dissipation range, which appears to extend well into the lower wave numbers thereby steepening the slope of the spectrum. The closeness of the power laws will require much higher Reynolds number data and improved statistics to discriminate between the two.

B. Anisotropy and inhomogeneous structure

The flow induced by RTI has much different character than that of homogeneous, isotropic turbulence and of RMI induced flows. The RTI flow is highly anisotropic, even at small scales because of constant gravitational acceleration. This is evidenced by the Taylor microscales and Reynolds numbers, defined in a manner that accommodates the anisotropic drive.

A microscale in the i direction can be defined as [13,26]

$$\lambda_i = \frac{\sqrt{\langle u_i^2 \rangle_{xy}}}{\sqrt{\langle \partial u_i / \partial x_i \rangle_{xy}^2}}^{1/2}$$

with statistics computed in the $(z = 0)$ plane. With statistical isotropy in the $(z = 0)$ plane, the x and y microscales are very close and can be averaged to define a single horizontal microscale,

$$\lambda_{xy} = \frac{\lambda_x + \lambda_y}{2}.$$

Fig. 8 illustrates [24] the temporal growth of the vertical and horizontal Taylor microscale in the $(z = 0)$ plane. The vertical and horizontal scales both grow as the bubbles increase in size, broadening the velocity correlation functions. The difference between the vertical and horizontal correlations give a direct measure of anisotropy in the flow. The ratio of these two correlation ranges grows to a maximum value of about 3.7 during diffusive growth and asymptotes to a value around 1.4 in the far nonlinear regime.

The Taylor microscale based Reynolds numbers can be defined as

$$\text{Re}_{\lambda,i} = \frac{\lambda_i \left[\langle u_i^2 \rangle_{xy} \right]^{1/2}}{\nu} \quad (\text{no sum on } i)$$

and again with spatial averages computed in the $(z=0)$ plane. The horizontal isotropy permits a horizontal Taylor Reynolds number to be defined as the average of $\text{Re}_{\lambda,x}$ and $\text{Re}_{\lambda,y}$,

$$\text{Re}_{\lambda,xy} = \frac{\text{Re}_{\lambda,x} + \text{Re}_{\lambda,y}}{2}.$$

Fig. 9 shows [24] that the anisotropy is also manifested in the Taylor scale Reynolds numbers.

C. Direct energy cascade and backscatter

The energy transferred across scales can be constructed from the Navier-Stokes equation. The major contributors are the production from gravity, the viscous dissipation, and the nonlinear transfer function. The production Π , transfer \mathbf{T} and dissipation \mathbf{E} spectra are plotted in Fig. 10 [24] on the z (inhomogeneous direction) versus $\log(k)$ (homogeneous plane) domain for several times. Early on, the peaks of the production and dissipation spectra are

close to one another since the flow was initialized from the rest. Later the production spectrum moves toward lower wave numbers from the production from the potential energy, whereas the peak of the dissipation spectrum roughly stays fixed. By the end of the simulation, there is some spectral separation between the two, i.e., as structures merge within the mixing layer, energy is deposited at larger scales.

Physically, the increasing separation of peaks between the production and dissipation spectra is a direct result of an increasing Reynolds number and an expanding inertial range for this developing flow. The transfer spectrum exhibits an intricate web of positive and negative regions interspersed over a wide range in z and k . At higher wave numbers T is mostly positive, indicating a net cascade of energy to smaller scales. It is also positive at the top and bottom of the mixing zone, suggesting vertical transport of energy to the bubble and spike fronts. Inside the mixing zone, backscatter appears approximately of equal importance to forward-scatter. It further appears that, at each instant in time, some z locations may be undergoing forward energy cascade, while neighboring regions are simultaneously experiencing inverse cascade.

IV. Scaling and spectra of RMI

Zhou [25] and Clark & Zhou [27] have presented an analysis that draws a connection between the scaling exponents of the mixing zone width and the growth of the length-scale in a decaying, weakly anisotropic turbulence. The physical picture is that of an initially quiescent flow field subject to an impulsive injection of energy (perhaps at all scales) which is then allowed to freely decay. Despite the strong anisotropy and lack of an equilibration of the statistical quantities at early time, it is clear that the analogy between the RM induced flow and

decaying isotropic turbulence improves as the shock-induced anisotropic flow tends toward isotropy long after the shock passes. This is quite different from the cases of RTI or KHI flows where the driving force is always present.

While the evolution in the case of a single-mode RMI induced flow is understood relatively well, here we focus instead on the late stages of the evolution of the RM mixing layer initiated from a multi-modal initial condition. The leading order characterization is of the width of the mixing layer as a function of time, and more specifically the “bubble” (light fluid penetrating heavier fluid) and “spike” (heavy fluid penetrating lighter fluid) growth rates

$$h_i \sim t^{\theta_i}$$

where $\theta_S = \theta_B(1 + A)$. Alon et al [28] reported that $\theta_B = 0.4$ and more recently Oron et al. [29] found that $\theta_B = 0.2$.

The fact that the mixing zone width is the largest observable feature of the flow suggests the importance of a dominant large length scale, which, in turn, is associated with the low-wave number power-law of the energy spectrum according to more than a half century of turbulence theory [25,27]

$$h_{B,S} = \lambda_{B,S} \frac{t^{\theta} + t_{B,S}}{t_0}$$

where t_B and t_S are the virtual time origin, the coefficients λ_B and λ_S set the amplitude of the mixing –layer scaling laws. Here $\theta = 2 / (m + 3)$ where m is the exponent of the energy spectrum at low-wave number $E(k) \sim k^m$.

The low-wave number behavior of a turbulent flow is related to the evolution of the largest scales in the flow field (i.e., velocity correlations at large physical distances).

The values of θ can now be obtained by substituting the exponent of low-wave number energy spectrum. Batchelor assumed that $m = 4$ for an isotropic decay. Lesieur and Schertzer [30] pointed out that the case of $m > 4$ is modified by backscatter to $m = 4$.

Saffman [31] showed that for a homogeneous field generated by an impulsive force, $m = 2$ and that the large-scale structure is an invariant of the flow field (i.e., the “permanence of big eddies”). This case corresponds to an equipartition of energy at the large-scales, implying that the turbulence (i.e., some realizations within the statistical ensemble of turbulent realizations) must possess a net momentum.

Speziale and Bernard [32] studied the Kàrmàn-Howarth equation in an effort to deduce the fully self-similar form of decaying isotropic turbulence with viscosity. Clark and Zemach [33] concurred that such a solution, if it exists, is fully self-similar, but point out that this corresponds to a low wave number exponent of $m = 1$. However, this seems physically unreasonable since a value of $m < 2$ corresponds to a modal energy spectrum that is singular at the origin.

Hence, it would be reasonable to only consider the cases of $2 < m \leq 4$, which correspond to $2/7 < \theta \leq 2/5$, consistent with the LEM measurements and values presented by references [28]-[29].

This investigation has significant implications on the role of the time origin in scaling RMI flows. The exponent θ is function of the low-wave number part of the energy spectrum (i.e., the largest physical scales) and thus must be shared across the mixing layer after being initially established by the shock passage. This “restricted” view of the exponent dependencies then requires that differences in the behaviors be due to the virtual time origins and amplitudes. Figs. 11-12 demonstrated this case.

As pointed out already, the mixing layer may become highly turbulent, during which time two-point measurements are needed for a more complete statistical description of the flow.

For turbulent flow induced by RMI, the energy spectrum can be found using the same procedure as that applied to RTI flow [25]

$$E(k, z) = C_{RM} A V \varepsilon^{\frac{1}{3}} k^{-3/2}$$

Here, C_{RM} is a constant. Although the scaling exponents do not change significantly from the Kolmogorov “-5/3 law,” we stress that the prefactor now depends on the parameters Atwood A and the change in the interface velocity induced by the shock wave V . The theoretical prediction is for the external time scale dominated regime; for late time when flow becomes essentially freely decaying turbulence, a transition to the steeper Kolmogorov spectrum is expected.

Cohen et al. [34] conducted a three dimensional simulation of a RMI flow (up to 8 billion zones) using sPPM. The calculation is motivated by the shock tube experiment of Vetter and Sturtevant [35]. It was found that the exponent of the energy spectrum’s wave number dependence in the inertial range is around 1.19, so it is less steep than either a Kolmogorov spectrum or that of Zhou [25]. Two possible reasons were identified: (1) strong numerical dissipation; (2) the two-length-scale nature of the experiment.

*This work was performed under the auspices of the U.S. Department of Energy by the University of California Lawrence Livermore National Laboratory under contract No. W-7405-Eng-48.

Reference:

- [1]. Lord Rayleigh, *Proc. Roy. Math. Soc.*, **14**, 170 (1883);
Lord Rayleigh, *Phil. Mag.* **6**, **xxi**, 697, (1911);
G.I. Taylor, *Proc. R. Soc. London*, Ser A, **201**, 192 (1950)
- [2] R.D. Richtmyer, *Comm. Pure Appl. Math*, **13**, 297 (2001);
E.E. Meshkov, *Izv. Akad. Sci., USSR Fluid Dyn.*, **4**, 101 (1969).
- [3] L. Smarr, J.R. Wilson, R.P. Barton, R.L. Bowers, *Astrophys. J.*, **246**, 511 (1981)
- [4] W.D. Arnett, J.N. Bahcall, R.T. Kirshner, and S.E. Woosley, *Annu. Rev. Astron. Astrophys.*, **27**, 629 (1989)
- [5] B. A. Remington, R.P. Drake, H. Takabe, D. Arnett, *Phys. of Plasma*, **7**, 1641 (2000)
- [6] J. Lindl, *Inertial Confinement Fusion: The quest for ignition and energy gain* (Springer, NY 1997)
- [7] P.E. Dimotakis, *J. Fluid Mech.*, **409**, 69, (2000)
- [8] G. K. Batchelor, *The Theory of Homogeneous Turbulence*, (Cambridge University Press, Cambridge, 1953).
- [9] Y. Zhou, Harry F. Robey, Alfred C. Buckingham, *Phys. Rev. E*, (submitted, 2002)
- [10] Robey, Zhou, Buckingham, et al. Submitted to *Phys. Plasma* (2002)
- [11] G.G. Stokes, *Trans. Cambr. Phil. Soc.* **9**, *Part II*. 8-106. (Reprinted): (1901): *Math. & Phys. Papers*, **3**, Cambr. Univ. Press, London and New York. 1-141.
- [12] H. Lamb, *Hydrodynamics*, Dover, N.Y., 619-620, (1911).
- [13] H. Tennekes, and J.L. Lumley, *First Course in Turbulence* (MIT Press, Cambridge, MA, 1972)
- [14] H. Schlichting, *Boundary-Layer Theory*, (McGraw-Hill, New York, 1951)
- [15] K.I. Reed, *Physica D*, **12**, 45 (1984)
- [16] D.L. Youngs, *Physica D*, **12**, 32 (1984);
- [17] K.I. Reed and D.L. Youngs, AWE report (unpublished, 1993)
- [18] M.B. Schneider, G. Dimonte, and B. Remington, *Phys. Rev. Lett.* **80**, 3507 (1998).
- [19] G. Dimonte and M. Schneider, *Physics of Fluids*, **12**, 304 (2000).
- [20] Rightley, Vorobieff, Martin and Benjamin, *Phys. Fluids*, **11**, 186 (1999)
- [21] S.I. Braginskii, in *Review of Plasma Physics*, (Consultants Bureau, New York, 1965)
- [22] NRL Plasma Formulary
- [23] J.G. Clerouin, M.H. Cherifi, and G. Zerah, *Europhys. Lett.*, **42**, 37 (1998)

- [24] A.W. Cook and Y. Zhou, *Phys. Rev. E*, **66**, 026312 (2002)
- [25] Y. Zhou, *Phys. Fluids*, **13**, 538 (2001).
- [26]. K.K. Nomura and S.E. Elghobashi, *Theoret. Comput. Fluid Dynamics*, **5**, 153 (1993).
- [27] T.T. Clark and Y. Zhou, Submitted to *Phys. Fluids*, 2002
- [28] U. Alon, J. Hecht, D. Ofer, and D. Shvarts, *Phys. Rev. Lett.*, **74**, 534 (1995).
- [29] D. Oron, L. Arazi, D. Kartoon, A. Rikanati, U. Alon, and D. Shvarts, *Phys. Plasma*, **8**, 2883 (2001).
- [30] M. Lesieur and D. Schertzer, *J. Mec.*, **17**, 609 (1978).
- [31] P.G. Saffman, *J. Fluid Mech.*, **27**, 581 (1967).
- [32] C.G. Speziale and P.S. Bernard, *J. Fluid Mech.* **241**, 645 (1992).
- [33] T.T. Clark and C. Zemach, *Phys. Fluids*, **10**, 2846 (1998).
- [34] R. Cohen, W.P. Dannevik, A.M. Dimits, D.E. Eliason, A.A. Mirin, Y. Zhou, D.P. Porter, and P.R. Woodward, *Phys. Fluids*, **14**, 3692 (2002)
- [35] M. Vetter and B. Sturtevant, Experiments on the Richtmyer-Meshkov instability of an air/ SF_6 interface, *Shock Waves*, **4**, 247 (1995)

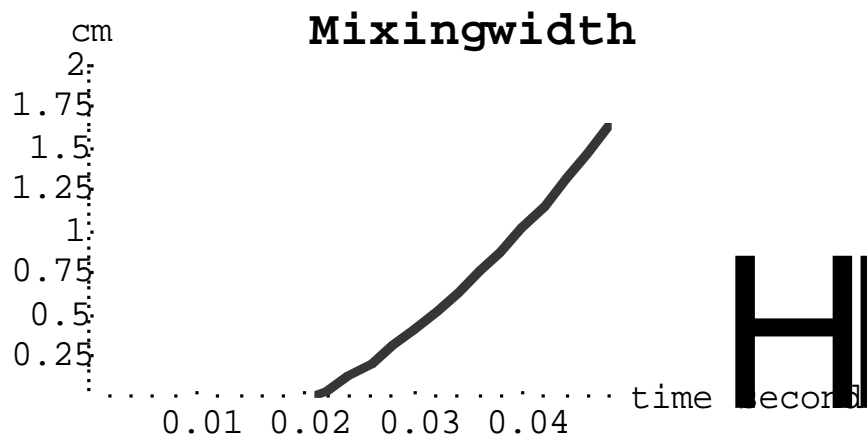


Fig. 1. a

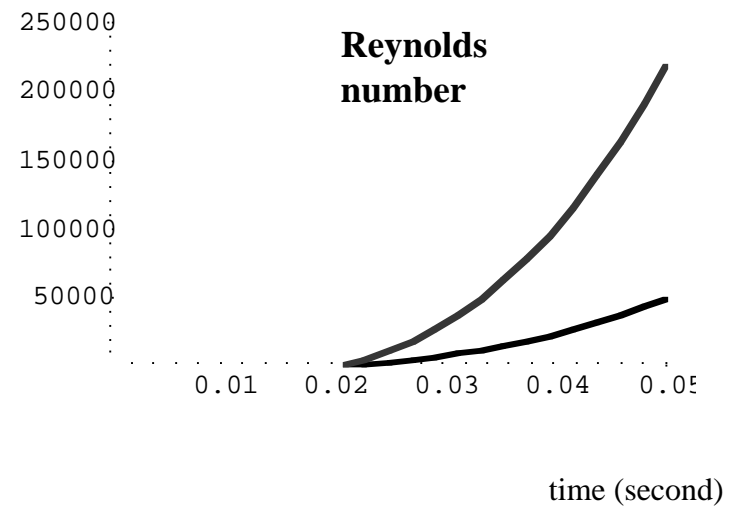


Fig. 1. b

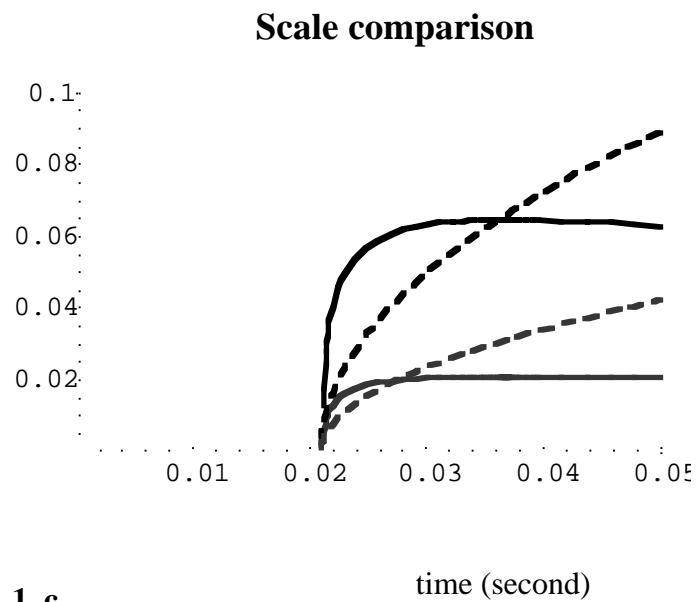


Fig. 1. c

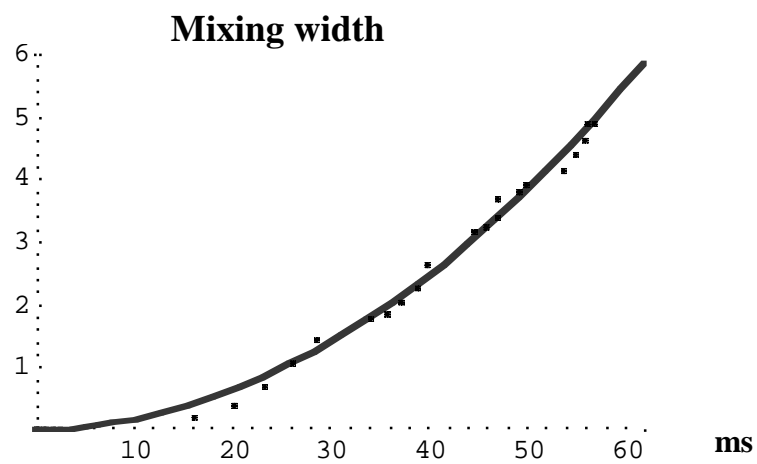


Fig. 2 a

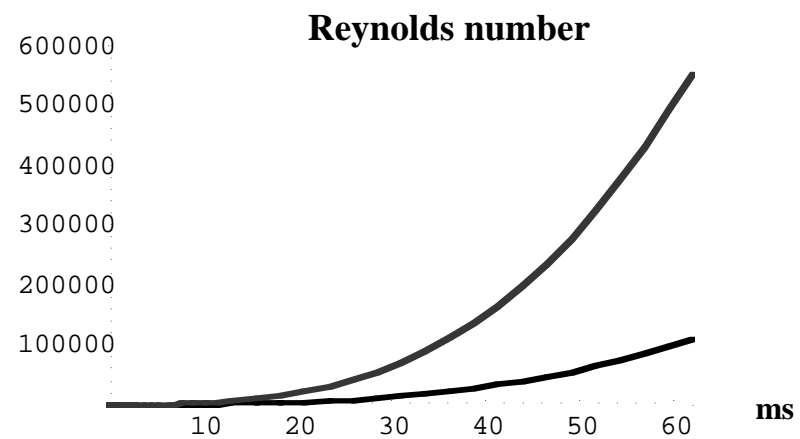


Fig. 2 b

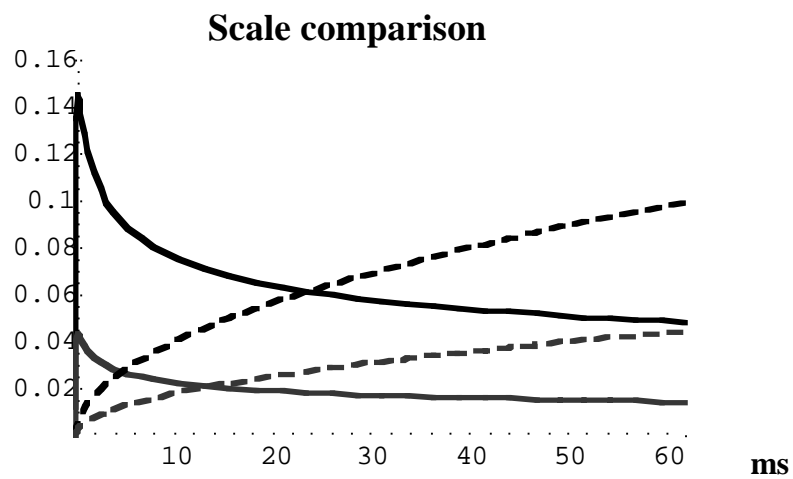


Fig. 2c

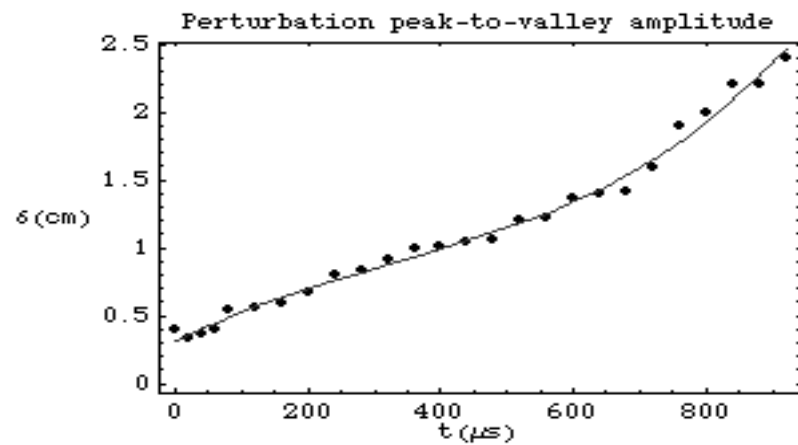


Fig. 3 a

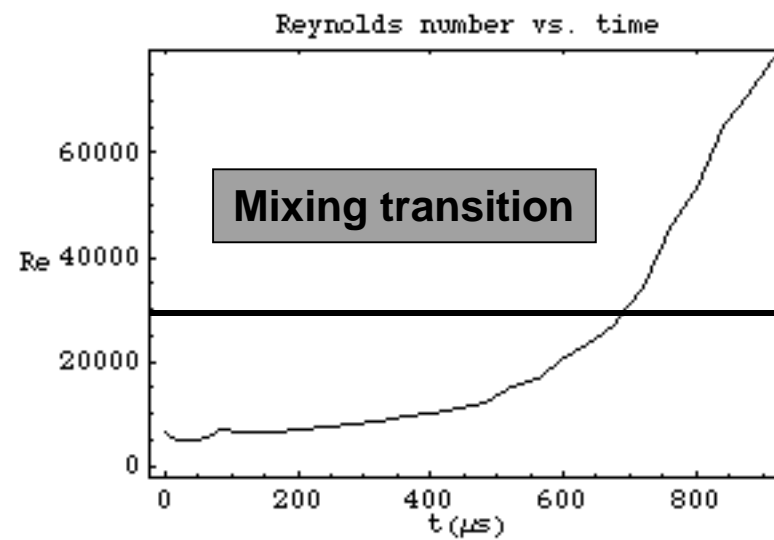


Fig. 3 b

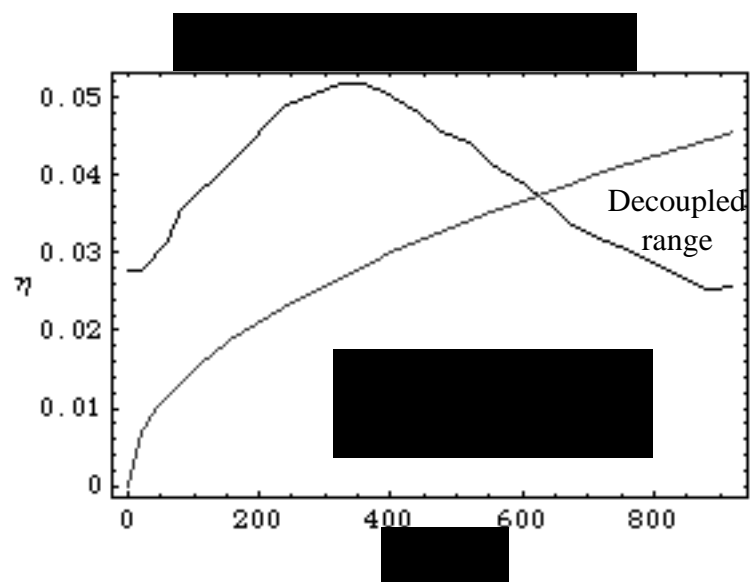


Fig. 3c

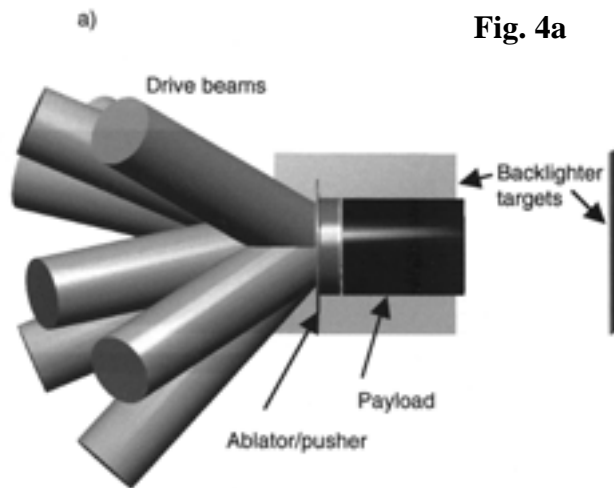


Fig. 4a

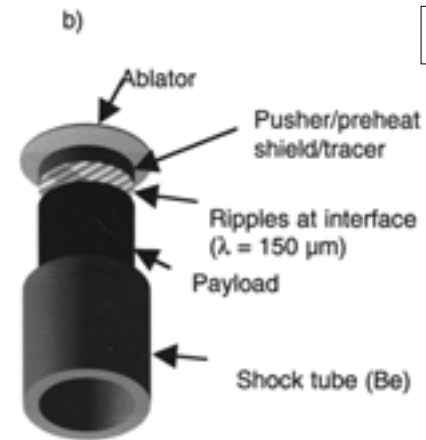


Fig. 4b

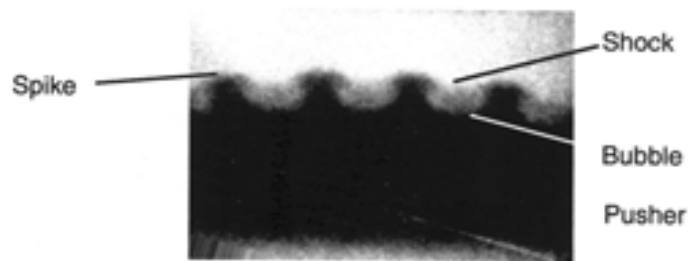


Fig. 4 c

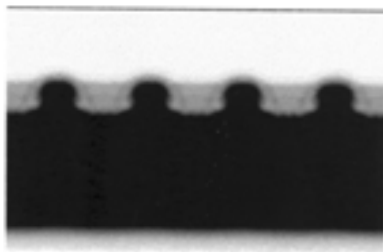


Fig. 4 d

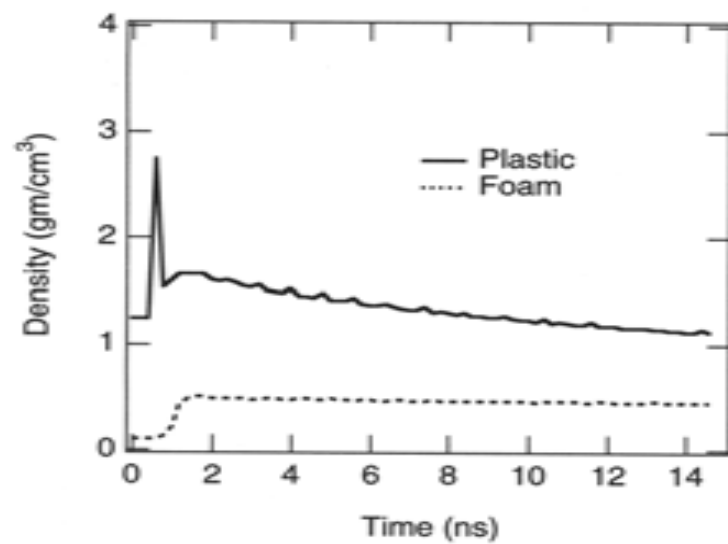


Fig. 4 e

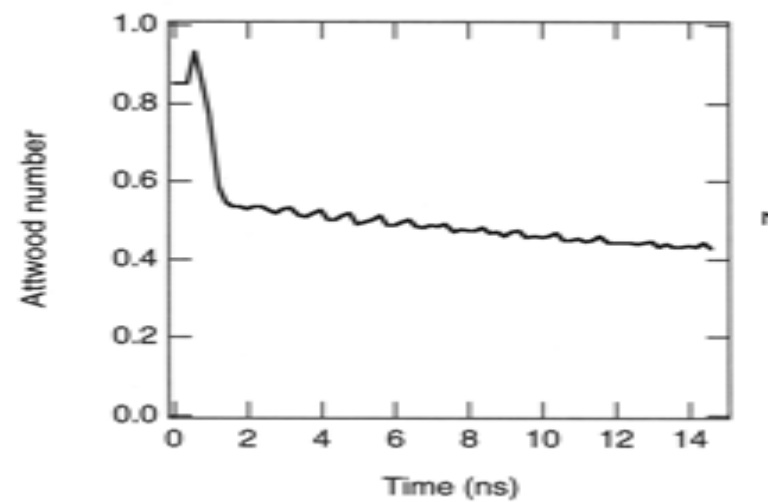


Fig. 4 f

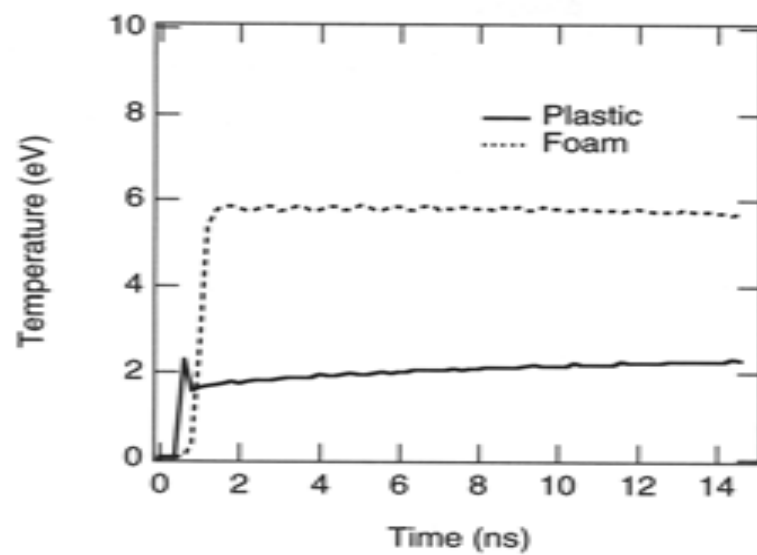


Fig. 4 g

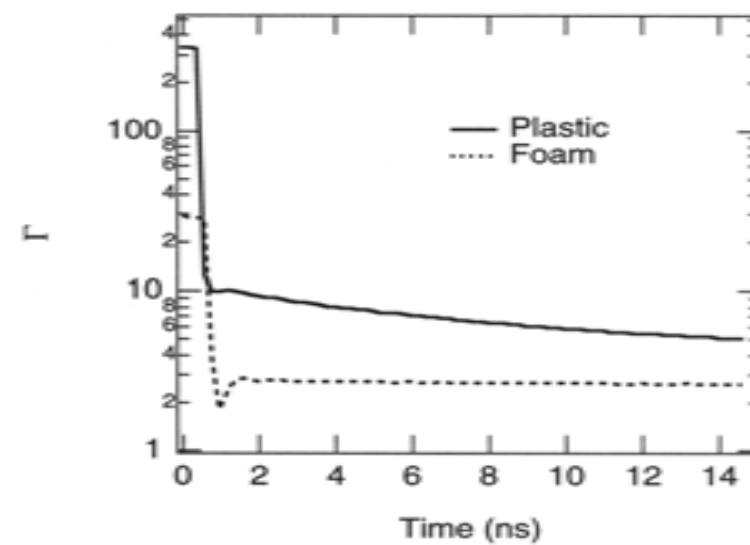


Fig. 4 h

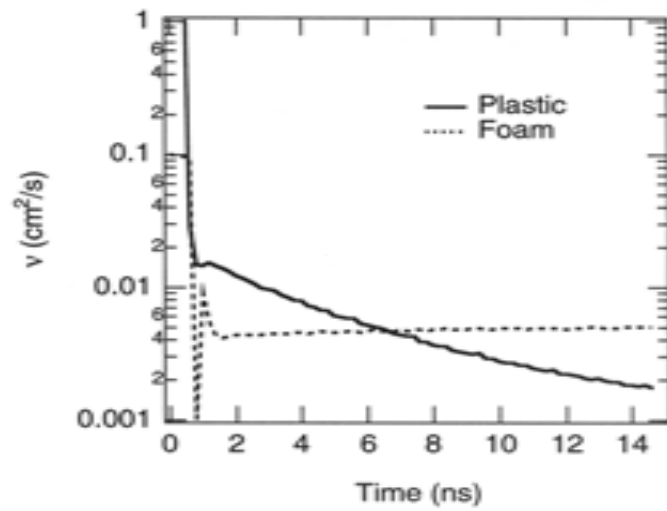


Fig. 4 i

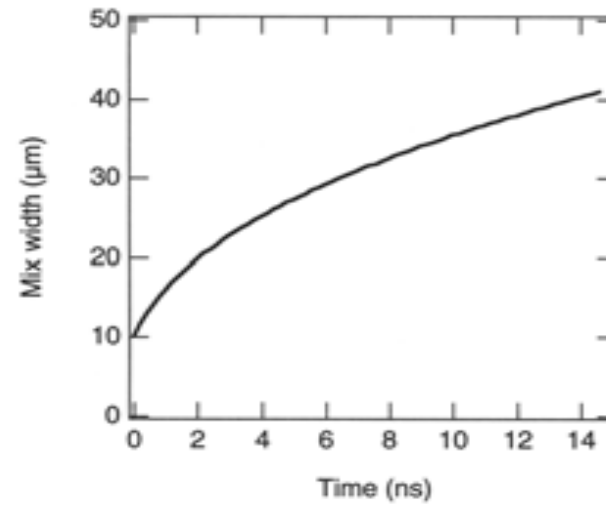


Fig. 4 j

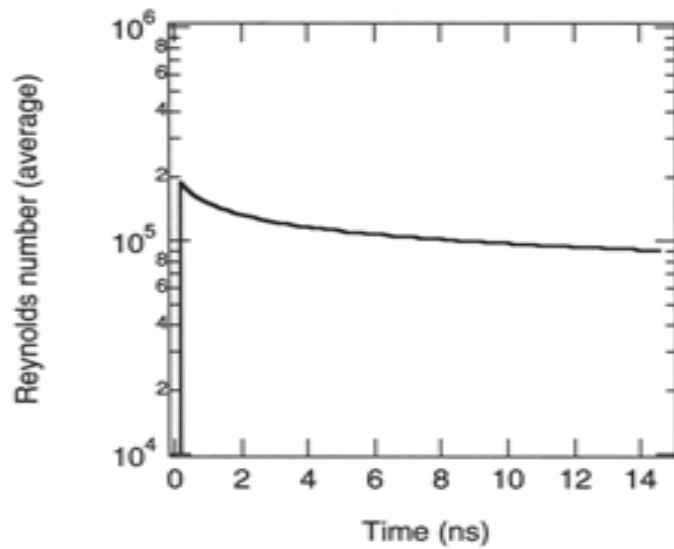
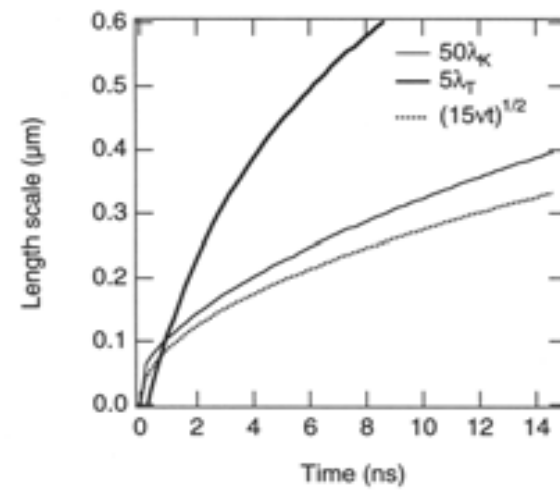


Fig. 4 k



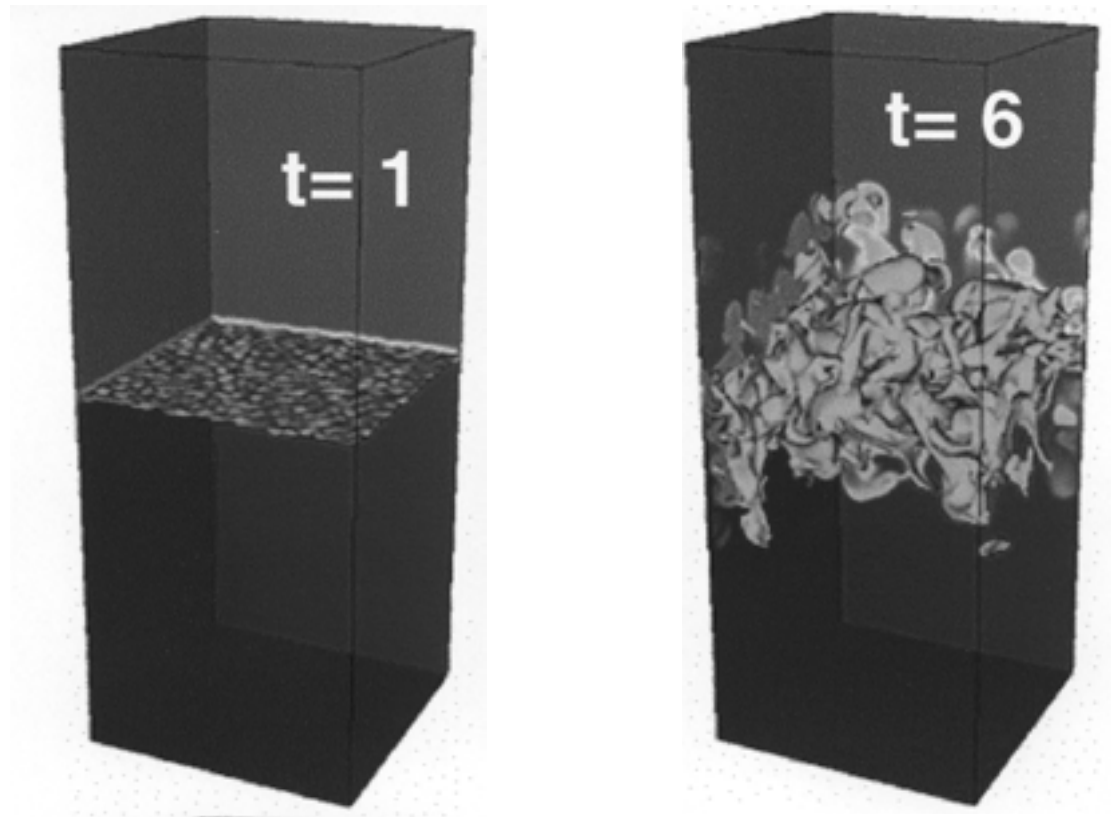


Fig. 5

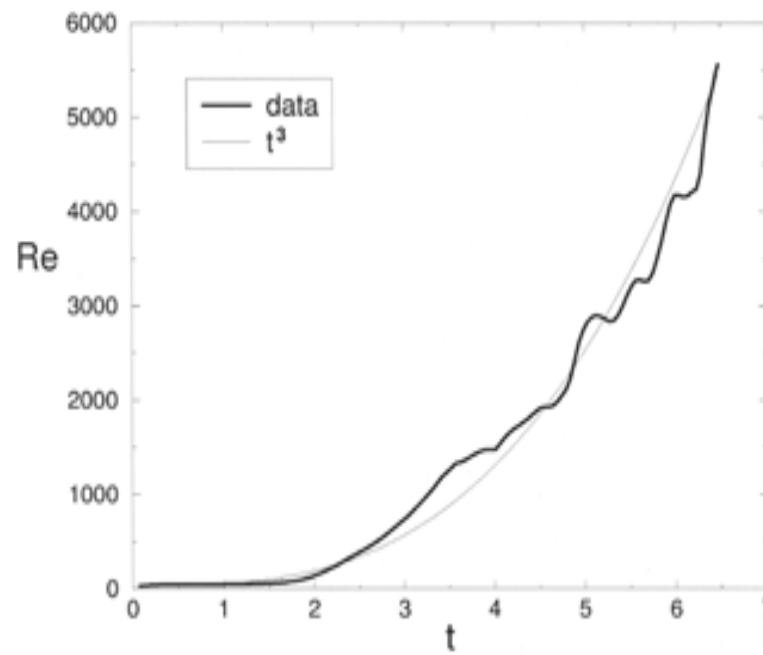


Fig. 6

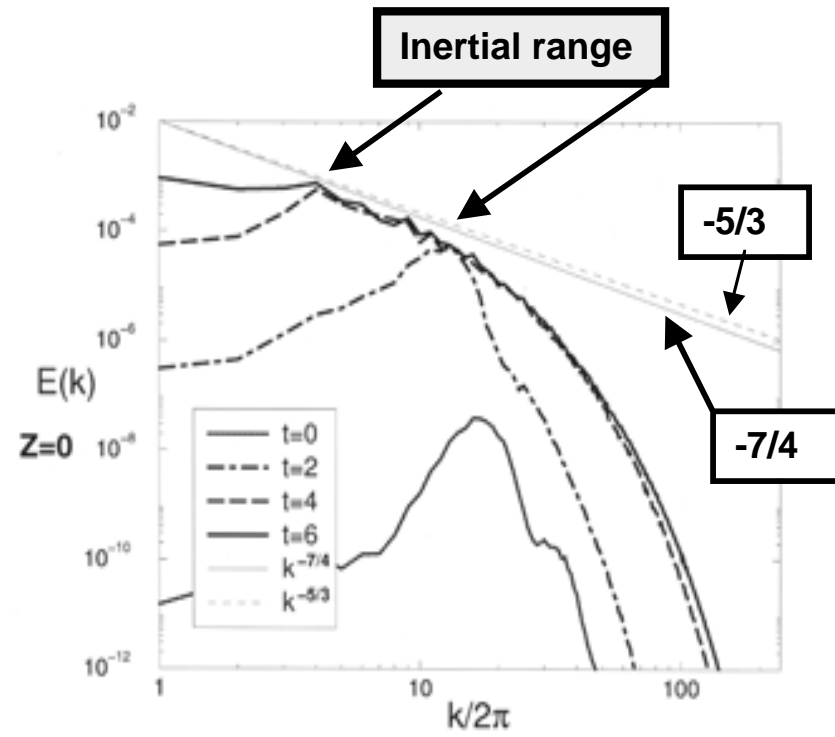


Fig. 7

Taylor microscale

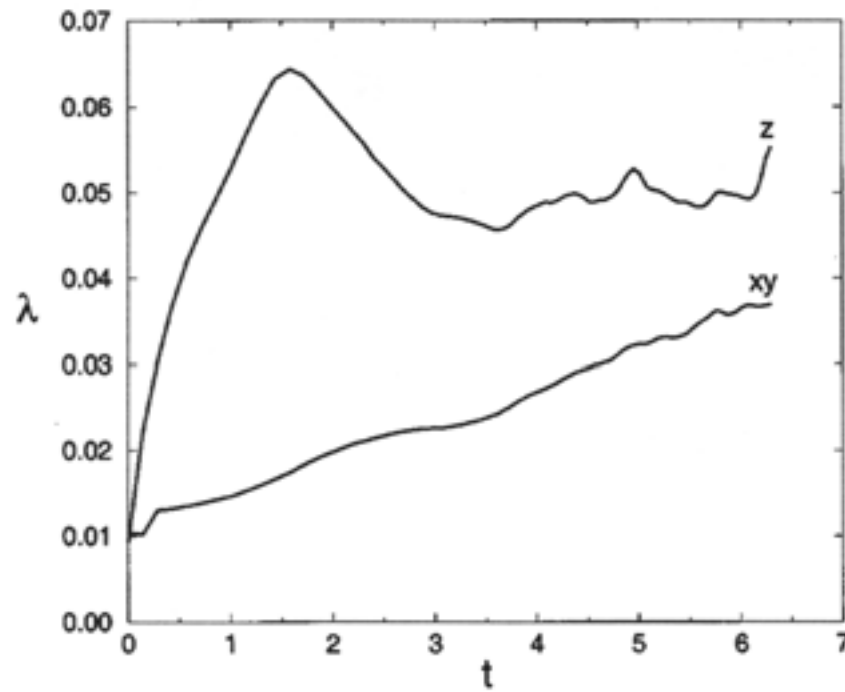


Fig. 8

Re based on Taylor microscale

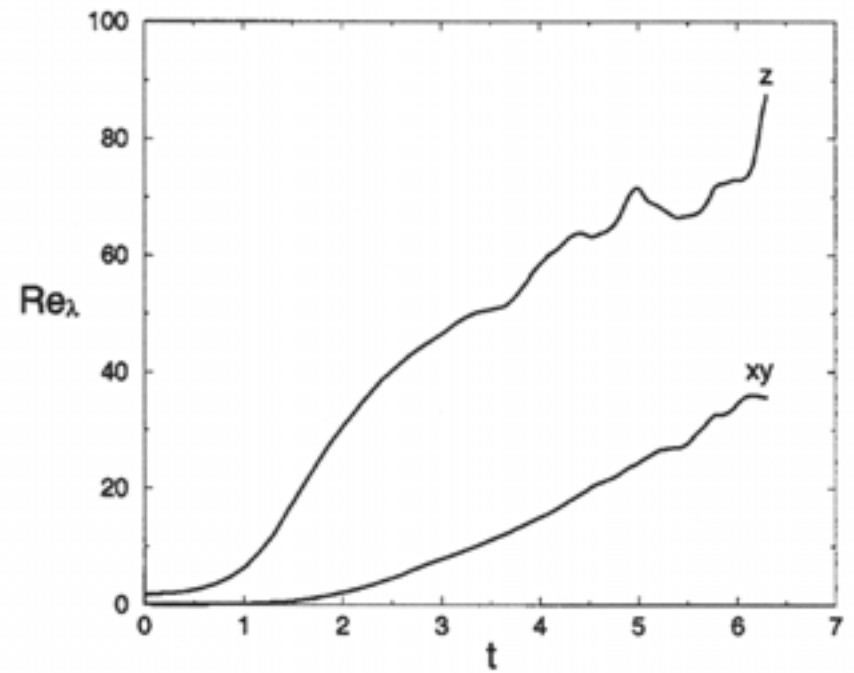


Fig. 9

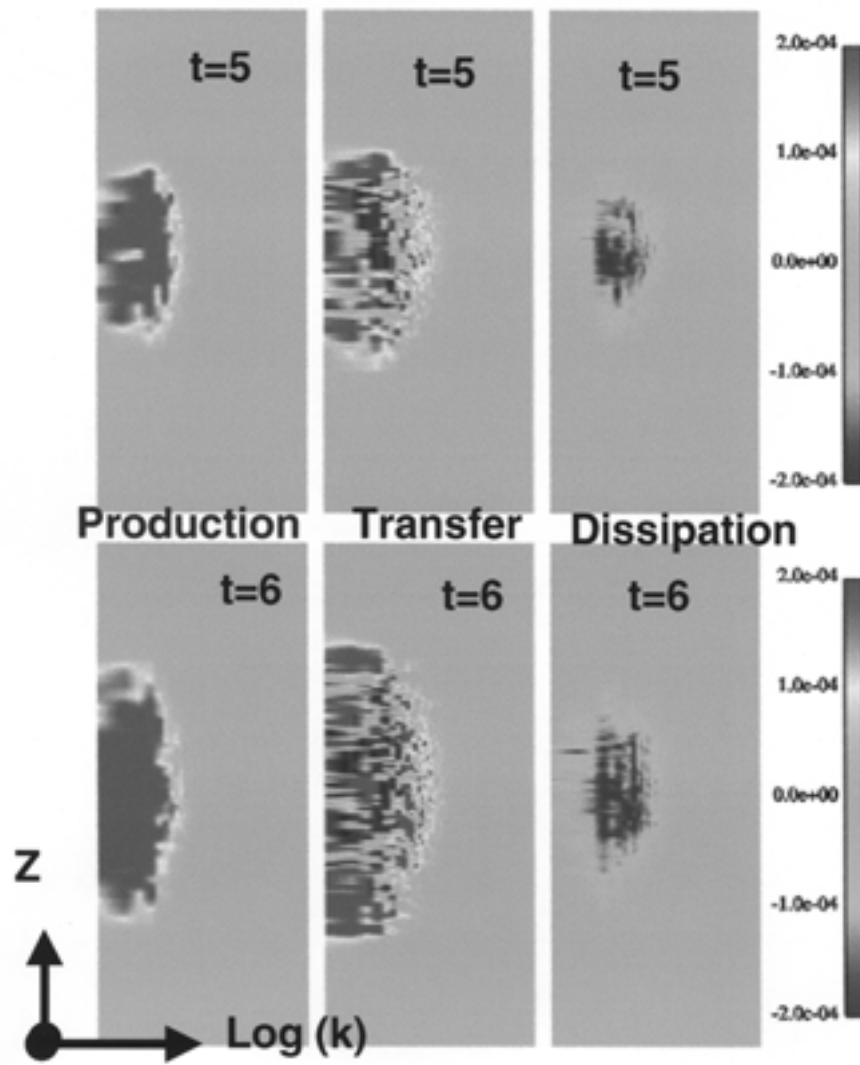


Fig. 10

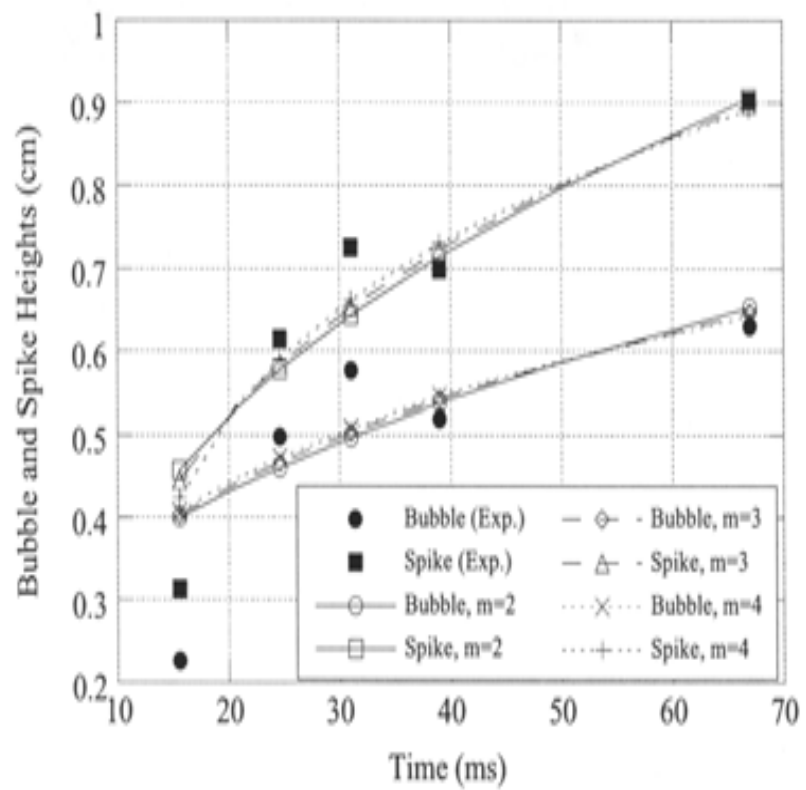


Fig. 11

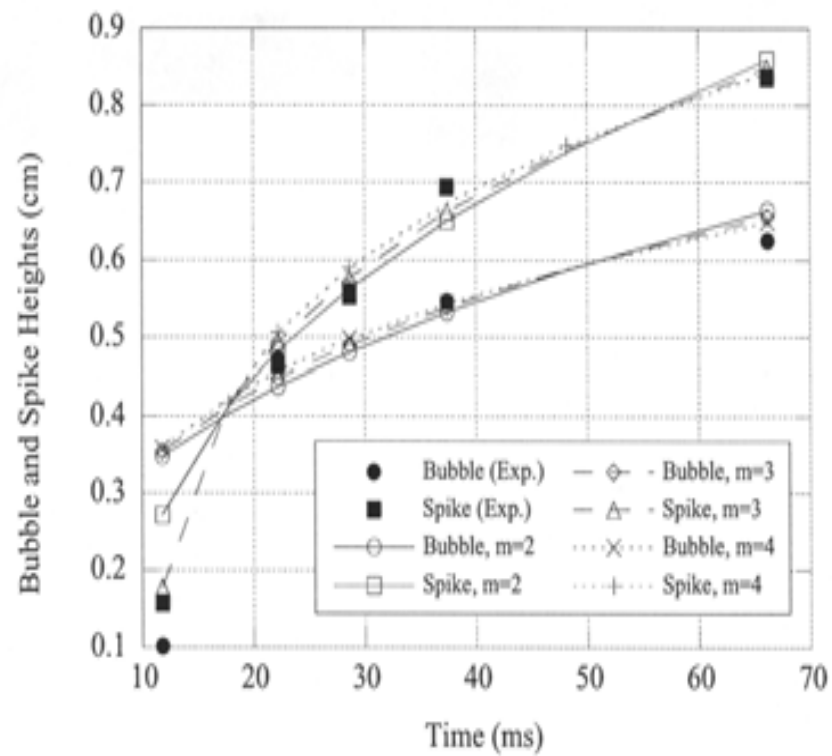


Fig. 12